

# Gravitational microlensing of AGN dusty tori

Marko Stalevski<sup>1,2,3\*</sup>, Predrag Jovanović<sup>1,3</sup>, Luka Č. Popović<sup>1,3</sup>  
and Maarten Baes<sup>2</sup>

<sup>1</sup>*Astronomical Observatory, Volgina 7, 11060 Belgrade, Serbia*

<sup>2</sup>*Sterrenkundig Observatorium, Universiteit Gent, Krijgslaan 281-S9, Gent, 9000, Belgium*

<sup>3</sup>*Isaac Newton Institute of Chile, Yugoslavia Branch, Volgina 7, 11060 Belgrade, Serbia*

10 August 2012

## ABSTRACT

We investigated gravitational microlensing of active galactic nuclei dusty tori in the case of lensed quasars in the infrared domain. The dusty torus is modeled as a clumpy two-phase medium. To obtain spectral energy distributions and images of tori at different wavelengths, we used the 3D Monte Carlo radiative transfer code SKIRT. A ray-shooting technique has been used to calculate microlensing magnification maps. We simulated microlensing by the stars in the lens galaxy for different configurations of the lensed system and different values of the torus parameters, in order to estimate (a) amplitudes and timescales of high magnification events, and (b) the influence of geometrical and physical properties of dusty tori on light curves in the infrared domain. We found that, despite their large size, dusty tori could be significantly affected by microlensing in some cases, especially in the near-infrared domain (rest-frame). The very long time-scales of such events, in the range from several decades to hundreds of years, are limiting the practical use of this method to study the properties of dusty tori. However, our results indicate that, when studying flux ratios between the images in different wavebands of lensed quasars, one should not disregard the possibility that the near and mid-infrared flux ratios could be under the influence of microlensing.

**Key words:** gravitational lensing: micro – galaxies: active – infrared: galaxies.

## 1 INTRODUCTION

Gravitationally lensed systems with multiple images represent a powerful tool to study the structure of both the galaxy which acts as the lens and the background source. In a number of lensed systems in which a quasar is the source, the flux ratios between the lensed images deviate from those predicted by the simple lens models (see e.g. Kochanek 1991; Keeton et al. 2003; Goldberg et al. 2010). The fluxes, in different wavebands, can be contaminated by different effects such as microlensing by the stars (e.g. Schneider & Wambsganss 1990) or millilensing by a massive structure in the lens galaxy (e.g. Mao & Schneider 1998), dust extinction (e.g. Elíasdóttir et al. 2006) and also by the time delay itself (e.g. Popović & Chartas 2005). Consequently, the flux ratio anomaly observed in some lensed quasars can be caused by extinction and/or gravitational microlensing/millilensing (see e.g. Popović & Chartas 2005; Yonehara et al. 2008).

The size of the source has a large effect on the fluctuations due to microlensing. As a large extended source covers a larger area of a microlensing magnification pattern in the source plane at any given time than a small source, its brightness varies less as it moves relative to the lens and observer (Mortonson et al. 2005). As a general

rule, the variability of a lensed source is significantly affected by microlensing only if the source is smaller than the relevant length scale - the projection of the Einstein radius of a microlens on to the source plane (Courbin et al. 2002). Since the sizes of different emitting regions of quasar are wavelength-dependent, microlensing by the stars in the lens galaxy will lead to a wavelength-dependent magnification. The X-ray radiation is coming from the very compact region in the innermost part of the accretion disk, and therefore, it will be magnified more than the radiation in the UV and optical bands, coming from outer, larger parts of the disk. Thus, although the phenomenon of gravitational lensing is achromatic, due to the complex structure of emission regions, “chromatic” effect may arise in a lensed quasar system (see e.g. Popović & Chartas 2005; Jovanović et al. 2008; Mosquera et al. 2009, 2011). The “chromaticity” in lensing effect can be used to investigate both, an unresolved structure of the innermost region of quasars (see e.g. Wyithe et al. 2002; Abajas et al. 2002; Popović et al. 2003, 2006; Bate et al. 2008; Mosquera et al. 2009; Dai et al. 2010; Blackburne et al. 2011; Garsden et al. 2011) and the structure of the lens galaxy (see e.g. Inoue & Chiba 2005; Chiba et al. 2005; Xu et al. 2010). Moreover, comparing flux ratios at different wavelengths makes it possible to constrain the amount of micro- and milli-lensing present in the system, and the sizes of the perturbers (see e.g. Goldberg et al. 2010).

\* E-mail: mstalevski@aob.rs (MS)

Since the X-ray and UV/optical radiations are coming from relatively compact regions (from several light-days to a light-month), the flux ratios in these wavebands are sensitive to both microlensing by the stars and millilensing by a cold dark matter (CDM) substructure (see e.g. [Metcalf & Madau 2001](#); [Popović & Chartas 2005](#); [Dobler & Keeton 2006](#); [Jovanović et al. 2008](#); [Goldberg et al. 2010](#); [Xu et al. 2010](#)). On the other hand, the infrared (IR) emitting region of a quasar is assumed to be a toroidal structure of dust, with dimensions significantly larger than the the projection of the Einstein radius of a microlens on to the source plane. Therefore one would expect that the IR radiation of lensed quasars would only be affected by the relatively massive subhalos (millilensing) (see [Inoue & Chiba 2005](#); [Chiba et al. 2005](#); [Sluse et al. 2006](#); [Yonehara et al. 2008](#); [Minezaki et al. 2009](#); [Xu et al. 2010](#); [Fadely & Keeton 2011](#)). However, certain geometrical and physical properties of the dusty torus can conspire to allow non-negligible microlensing effects in the infrared domain.

Infrared spectra of most quasars are dominated by thermal emission from hot dust in their tori, or alternatively, by nonthermal synchrotron emission from the regions near their central black holes ([Agol et al. 2000](#)). Variability in the infrared band due to gravitational microlensing could be used to constrain the size of the infrared emission region, and hence to distinguish between the thermal and synchrotron mechanisms. If the infrared radiation varies on timescales shorter than decades, then its emission region is smaller, located closer to the central black hole, and its emission is non-thermal, while longer timescales indicate a larger, thermal region ([Neugebauer & Matthews 1999](#)). Additionally, chromatic effects in the infrared band have been observed in some of the lensed quasars, where the color differences between their multiple images were detected ([Yonehara et al. 2008](#)). The most realistic scenario that can explain the observed color differences is gravitational microlensing, in contrast to the dust extinction and the intrinsic variability of quasars ([Yonehara et al. 2008](#)).

Some previous theoretical and observational studies suggested that the infrared emission of quasars is not significantly affected by microlensing, implying that it is most likely produced in their dusty tori. For instance, [Agol et al. \(2000\)](#) studied the mid-IR emission of Q2237+0305 observed by Keck and found that it was not affected by microlensing, which ruled out the synchrotron mechanism and supported the model with hot dust extended on a length scale of more than 0.03 pc. [Wyithe et al. \(2002\)](#) used mid-IR and V-band flux ratios for images *A* and *B* of Q2237+0305 to infer the size of the mid-IR emission region and found that it was comparable to or larger than the Einstein Ring Radius (ERR) of the microlens, and hence at least two orders of magnitude larger than the optical emission region. They used simple Gaussian and annular intensity profiles of the dusty torus and found that the results were dependent on the assumed source profile ([Wyithe et al. 2002](#)). Recent Spitzer observations of the same gravitationally lensed quasar ([Agol et al. 2009](#)) showed that a dusty torus model with a small opening angle could satisfactorily explain the shape of the observed infrared SED, excluding an offset in wavelength of the silicate feature. However, the same authors found that the near-IR fluxes are increasingly affected by microlensing toward shorter wavelengths and that this wavelength dependence is consistent with a model in which a dusty torus and an accretion disk both contribute to the infrared radiation near  $1\ \mu\text{m}$  ([Agol et al. 2009](#)).

In this paper we present simulations of gravitational microlensing of active galactic nucleus (AGN) dusty tori in the infrared domain. We consider microlensing by stars in the lens galaxies, in the case of lensed quasar systems. We modeled the dusty

torus as a clumpy two-phase medium. To obtain spectral energy distributions and images of the torus at different wavelengths, we used the 3D radiative transfer code SKIRT. For generating microlensing magnification maps, a ray-shooting method was used. To take into account the size of the dusty tori (as they are larger than the Einstein ring radius of the microlens projected on the source plane), the simulated images of the tori are convolved with the magnification maps. We simulated microlensing magnification events for different configurations of the lensed system and different values of the torus parameters. The aims of this paper are to estimate (a) amplitudes and timescales of high magnification events, and (b) the influence of geometrical and physical properties of dusty tori on microlensing light curves in the infrared domain.

The paper is organized as follows. In Section 2 we give a description of our dusty torus model, the method we used to calculate microlensing magnification map, and the parameters we adopted in this study. In Section 3 we present and discuss the results of simulated microlensing light curves of the dusty torus. In Section 4 we outline our conclusions.

## 2 MODEL

### 2.1 The radiative transfer code SKIRT

We have used the radiative transfer code SKIRT to calculate spectral energy distributions (SED) and images of torus at different wavelengths. SKIRT is a 3D Monte Carlo radiative transfer code, initially developed to investigate the effects of dust extinction on the photometry and kinematics of galaxies ([Baes et al. 2003](#)). Over the years, the code evolved into a flexible tool that can model the dust extinction, including both absorption and scattering, and the thermal re-emission of dust, under the assumption of local thermal equilibrium (LTE) ([Baes et al. 2005a,b](#)). This LTE version of SKIRT has been used to model different environments, such as, circumstellar disks ([Vidal & Baes 2007](#)), clumpy tori around active galactic nuclei ([Stalevski et al. 2012](#)) and a variety of galaxy types ([Baes et al. 2010](#); [de Looze et al. 2010](#)). Recently, the code was adapted to include the emission from very small grains and polycyclic aromatic hydrocarbon molecules ([Baes et al. 2011](#)).

### 2.2 Dusty torus model

According to the AGN unification model, the central continuum source (accretion disk) is surrounded by the geometrically and optically thick toroidal structure of dust and gas with an equatorial visual optical depth much larger than unity. In order to prevent the dust grains from being destroyed by the hot surrounding gas, [Krolik & Begelman \(1988\)](#) suggested that the dust in torus is organized in a large number of optically thick clumps. This dusty torus absorbs the incoming radiation and re-emits it, mostly in the infrared domain.

The details of the model of torus we used in this work can be found in [Stalevski et al. \(2012\)](#); here we will present only some of its properties relevant for this study. We modeled the torus as a 3D two-phase medium with high-density clumps and low density medium filling the space between the clumps.

We approximate the obscuring toroidal dusty structure with a conical torus (i.e. a flared disk). Its characteristics are defined by (a) half opening angle  $\Theta$ , (b) the inner and outer radius,  $R_{\text{in}}$  and  $R_{\text{out}}$  respectively, and (c) the parameters  $p$  and  $q$  that describe the dust density distribution. The inner radius is calculated according

to the prescription given by Barvainis (1987),

$$\left(\frac{R_{\text{in}}}{\text{pc}}\right) \simeq 1.3 \left(\frac{L_{\text{AGN}}}{10^{46} \text{ erg s}^{-1}}\right)^{0.5} \left(\frac{T_{\text{sub}}}{1500 \text{ K}}\right)^{-2.8} \quad (1)$$

where  $L_{\text{AGN}}$  is the bolometric ultraviolet/optical luminosity emitted by the central source and  $T_{\text{sub}}$  is the sublimation temperature of the dust grains.

We describe the spatial distribution of the dust density with a law that allows a density gradient along the radial direction and with polar angle, as the one adopted by Granato & Danese (1994):

$$\rho(r, \theta) \propto r^{-p} e^{-q|\cos\theta|}, \quad (2)$$

where  $r$  and  $\theta$  are coordinates in the adopted coordinate system. The dust mixture consists of separate populations of graphite and silicate dust grains with a classical MRN size distribution (Mathis, Rumpl & Nordsieck 1977). The total amount of dust is fixed based on the equatorial optical depth at  $9.7 \mu\text{m}$  ( $\tau_{9.7}$ ). Dust is distributed on a 3D Cartesian grid composed of a large number of cubic cells. To generate a clumpy, two-phase medium, we apply the algorithm described by Witt & Gordon (1996). The larger clumps are formed by forcing high-density state into several adjoining cells.

### 2.2.1 Spectral energy distribution of the primary continuum source

The primary continuum source of dust heating is the intense UV-optical continuum coming from the accretion disk. A good approximation of its emission is a central, point-like energy source, emitting isotropically. Its SED is very well approximated by a composition of power laws with different spectral indices in different spectral ranges. The adopted values are:

$$\lambda L_{\lambda} \propto \begin{cases} \lambda^{1.2} & 0.001 \leq \lambda \leq 0.01 \\ \lambda^0 & 0.01 < \lambda \leq 0.1 \\ \lambda^{-0.5} & 0.1 < \lambda \leq 5 \\ \lambda^{-3} & 5 < \lambda \leq 50 \end{cases} \quad (3)$$

where  $\lambda$  is expressed in  $\mu\text{m}$ . These values have been quite commonly adopted in the literature, and come from both observational and theoretical arguments (see e.g., Schartmann et al. 2005).

### 2.2.2 Parameters of the dusty torus model

For the bolometric luminosity of the primary source (the accretion disk) we adopted the value of  $10^{12} L_{\odot}$  (e.g. Davis & Laor 2011). According to the Eq. (1), assuming a dust sublimation temperature of 1500 K, the corresponding value of the inner radius of the torus is  $R_{\text{in}} = 0.8 \text{ pc}$ . Recent observations of nearby AGN suggest that the size of tori is likely restricted to several parsecs (Alonso-Herrero et al. 2011; Ramos Almeida et al. 2011). It is arguable whether this holds also for the tori in AGNs at much larger redshifts (i.e. quasars). Preliminary results from a recent study of high redshift quasars by Leipksi & Meisenheimer (2012) suggest that the hot dust properties do not change significantly with either redshift or luminosity. Therefore, for the outer radius of torus we adopted the values of 3 and 10 pc. The half opening angle of the torus takes values of  $30^\circ$ ,  $50^\circ$  and  $70^\circ$ . For the dust density distribution parameters we adopted the following values:  $p = 0, 0.5, 1$  and  $q = 0, 1, 2$ . The relative clump size, defined as the ratio of the outer radius of the torus over the clump size, is  $\xi = 12.5$ . The equatorial optical depth (determining also the total amount of dust) is fixed at  $\tau_{9.7} = 5$ . We calculated each model at three inclinations,

$i = 0^\circ, 70^\circ, 90^\circ$ , where  $i = 0^\circ$  corresponds to face-on view (type 1 AGN), and  $i = 90^\circ$  to edge-on view (type 2 AGN). The emission for all models is calculated on an equally spaced logarithmic wavelength grid ranging from 0.001 to 1000  $\mu\text{m}$ .

### 2.3 Microlensing model

Different microlensing models can be used for explaining the observed microlensing phenomena in quasars, such as microlensing by an isolated compact object (Chang & Refsdal 1979, 1984), or by a number of microdeflectors located within an extended object – the model called “straight-fold caustic” (Schneider, Ehlers & Falco 1992). However, the most realistic model is the so-called microlensing map (pattern) or caustic network which is usually applied in order to obtain a spatial distribution of magnifications in the source plane (where the dusty torus of quasar is located), produced by randomly distributed stars in the lensing galaxy (for more details see e.g. Schneider, Ehlers & Falco 1992). The lensing galaxy can be assumed as thin when compared with the whole light path, since its extent in the direction of the optical axis is much smaller than the angular diameter distances between observer and lens, observer and source and lens and source. In such case the dimensionless lens equation reads (Schneider, Ehlers & Falco 1992):

$$\vec{y} = \vec{x} - \vec{\alpha}(\vec{x}), \quad (4)$$

where  $\vec{x}$  and  $\vec{y}$  are normalized image and source positions, respectively, and  $\vec{\alpha}(\vec{x})$  is the deflection angle due to light bending in the gravitational field of the lens. The deflection potential is then given by:

$$\psi(\vec{x}) = \frac{1}{\pi} \int \kappa(\vec{x}') \ln |\vec{x} - \vec{x}'| d^2 x', \quad (5)$$

and it is related to the deflection angle by:  $\vec{\alpha}(\vec{x}) = \nabla\psi(\vec{x})$  and to the dimensionless surface mass density  $\kappa$  by the 2-dimensional Poisson equation:  $\nabla^2\psi = 2\kappa$ . For a field of point masses with an external shear  $\gamma$  and a smooth mass distribution  $\kappa_c$ , the normalized lens equation (4) is usually written as (Kayser et al. 1986):

$$\vec{y} = \sum_{i=1}^N m_i \frac{\vec{x} - \vec{x}_i}{|\vec{x} - \vec{x}_i|^2} + \left[ \begin{array}{cc} 1 - \kappa_c + \gamma & 0 \\ 0 & 1 - \kappa_c - \gamma \end{array} \right] \vec{x}, \quad (6)$$

where the sum describes light deflection by the stars and the last term is a quadrupole contribution from the lensing galaxy. The total surface mass density or convergence can be written as  $\kappa = \kappa_* + \kappa_c$ , where  $\kappa_*$  represents the contribution from the compact microlenses. The magnification map for some specific microlensing event can be generated if the following two parameters are known: the convergence -  $\kappa$ , and the shear due to the external mass -  $\gamma$ .

For generating microlensing magnification maps we used a ray-shooting method (Kayser et al. 1986; Schneider & Weiss 1986, 1987; Wambsganss et al. 1990). In this method, rays are followed backwards from the observer through the lens plane, to the source plane. First, we generate a random star field in the lens plane based on the parameter  $\kappa$ . After that, we solve the Poisson equation  $\nabla^2\psi = 2\kappa$  in the lens plane numerically, so we can determine the lens potential  $\psi$  in every point of the grid in the lens plane. To solve the Poisson equation numerically one has to write its finite difference form:

$$\psi_{i+1,j} + \psi_{i-1,j} + \psi_{i,j+1} + \psi_{i,j-1} - 4\psi_{i,j} = 2\kappa_{i,j}. \quad (7)$$

Here we used the standard 5-point formula for the two-dimensional

Laplacian. The next step is the inversion of equation (7) using Fourier transforms. After some transformations we obtain:

$$\hat{\psi} = \frac{\hat{\kappa}_{mn}}{2(\cos \frac{m\pi}{N_1} + \cos \frac{n\pi}{N_2} - 2)}, \quad (8)$$

where  $N_1$  and  $N_2$  are dimensions of the grid in the lens plane. Now, using the finite difference technique, we can compute the deflection angle  $\vec{\alpha} = \nabla\psi$  in each point of the grid in the lens plane. After computing the deflection angle, we can map the regular grid of points in the lens plane, via lens equation, onto the source plane. These light rays are then collected in pixels in the source plane, and the number of rays in one pixel is proportional to the magnification due to microlensing at this point in the source plane. Due to the relative motion between the observer, lens and source, the magnification over time will change, and a light curve for a small, pointlike source can be found by tracing a path across the magnification map.

Apart from the convergence  $\kappa$  and shear  $\gamma$ , another input parameter is width of the microlensing magnification map expressed in units of the Einstein ring radius in the source plane. The Einstein ring radius in the lens plane is defined as

$$\text{ERR} = \sqrt{\frac{4Gm}{c^2} \frac{D_1 D_{\text{ls}}}{D_s}}, \quad (9)$$

and its projection in the source plane is:

$$R_E = \frac{D_s}{D_1} \text{ERR} = \sqrt{\frac{4Gm}{c^2} \frac{D_s D_{\text{ls}}}{D_1}}, \quad (10)$$

where  $G$  is the gravitational constant,  $c$  is the speed of light,  $m$  is the microlens mass and  $D_1$ ,  $D_s$  and  $D_{\text{ls}}$  are the cosmological angular distances between observer-lens, observer-source and lens-source, respectively.

### 2.3.1 Parameters of the microlensing magnification map

The microlensing magnification map is calculated for typical values of average surface mass density and shear,  $\kappa = \gamma = 0.4$ . The map has  $1156 R_E$  on a side. For a source fixed at redshift of  $z_s = 2$ , and for the lens at  $z_l = 0.05$  and  $0.5$ , this is equal to  $61.42$  and  $19.99$  pc in the source plane, respectively). The size of the map is chosen because of the large dimensions of the dusty torus compared to  $R_E$ . But this particular value is also chosen for numerical reasons – the pixel size has to be the same in the images of the torus and the magnification map. Thus, the size and resolution of the images of the torus and the magnification map cannot be chosen independently. A flat cosmological model is assumed, with  $\Omega_M = 0.27$ ,  $\Omega_\Lambda = 0.73$  and  $H_0 = 71 \text{ km s}^{-1} \text{ Mpc}^{-1}$ . The mass of microlens is taken to be  $1 M_\odot$  in all simulations.

## 3 RESULTS AND DISCUSSION

In this section, we first present the microlensing magnification map used in this study and demonstrate the wavelength dependency of the AGN dusty torus size. Then, the size of the torus is taken into account by convolving the magnification map with images of the torus at different wavelengths. Finally, we discuss light curves of simulated magnification events, the amplitudes and timescales of these events, and the influence of different torus parameters. Note that, throughout this paper, we always refer to the rest-frame wavelengths.

We calculated microlensing light curves for a source fixed

at a redshift of  $z_s = 2$ , while the lens galaxy redshift takes values of  $z_l = 0.05$  and  $0.5$ . The former value of lens galaxy redshift ( $z_l = 0.05$ ) roughly replicates the well-known lensed system Q2237+0305 (also known as the “Einstein cross”), which is particularly susceptible to microlensing. The redshift of the lens in this system ( $z_l = 0.04$ ) is so low that the apparent angular velocity of the microlenses, in projection on the plane of the sky, is much higher than in other systems. Moreover, the Einstein rings of these microlenses have a larger angular diameter, making it more likely that they are larger than the source (Courbin et al. 2002). The second value chosen for calculation of magnification map ( $z_l = 0.5$ ) represents a more typical value of lens galaxy redshift in lensed systems.

The microlensing magnification map shown in Fig. 1 is calculated for the case of  $z_l = 0.05$  (and other parameters as described in Section 2.3.1). The left panel represents the whole map, with  $\sim 61.42$  pc ( $1156 R_E$ ) on the side; for comparison, the sizes of the tori used in this study ( $R_{\text{out}} = 3$  and  $10$  pc) are indicated with two white circles. The right panel is a zoom-in of the region with a side of  $12$  pc, from which the light curve of the microlensing events is extracted (vertical white line). The distribution of magnification is highly non-linear, with regions of low and high magnification and with a maximum magnification along the sharp caustic lines. Magnification pattern is color coded, with blue, cyan, yellow, orange and red regions corresponding to increasingly higher magnification. When a source crosses a caustic, a large change in magnification is expected.

### 3.1 Wavelength dependency of torus size

In the top row of Fig. 2 we present images of the torus at different wavelengths. At shorter wavelengths, it is the radiation from the inner (and hotter) region that dominates. Thus, at near-infrared wavelengths, the torus appears much more compact compared to its physical outer radius. On the other hand, at longer wavelengths, the emission arises from the colder dust. As this colder dust is placed further from the centre, all the way to the outer radius, the torus will appear larger at longer wavelengths. Therefore, the size of the torus is wavelength dependent, as seen in the top row Fig. 2.

The microlensing magnification maps are calculated for point sources. As the dusty torus is larger than the typical size of microlens  $R_E$ , they have to be treated as extended sources. To take this into account, the magnification map shown in Fig. 1 is convolved with the images of the torus at the different wavelengths. The bottom row of Fig. 2 shows the magnification maps after convolution with the corresponding torus images from the top row.

### 3.2 Simulated light curves of microlensing events

#### 3.2.1 Wavelength dependence

In Fig. 3 we present light curves of magnification events at different wavelengths. The light curves are extracted from the magnification maps convolved with the corresponding images of the tori, along the path shown in the right panel of Fig. 1 (starting from bottom, going to the top). The parameters of the torus are the same as taken in Fig. 2. The left panel of Fig. 4 illustrates the dependence of the absolute magnification amplitude on wavelength, for the prominent high magnification events (HME), peaking at  $\sim 3.3$  and  $\sim 2.3$  pc (indicated with a dotted line in the left and right panel of Fig. 3, respectively). From these figures we see that, as a consequence of the



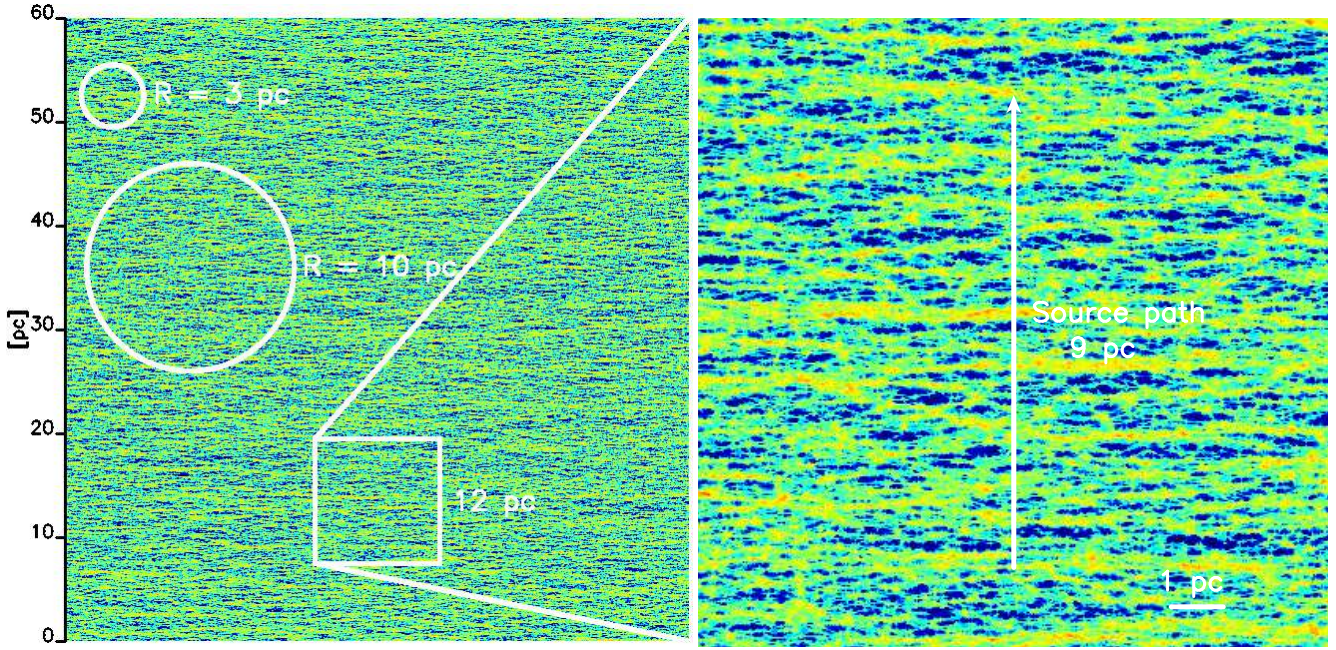


**Figure 1.** *Left panel:* Microlensing magnification map, with 61.42 pc ( $1156 R_E$ ) on the side. Average surface mass density and shear take value of  $\kappa = \gamma = 0.4$ . White circles indicate sizes of tori used in this study ( $R_{\text{out}} = 3$  and 10 pc). *Right panel:* zoom-in on the square with 12 pc on the side, from which the light curve of microlensing event is extracted (vertical white line).

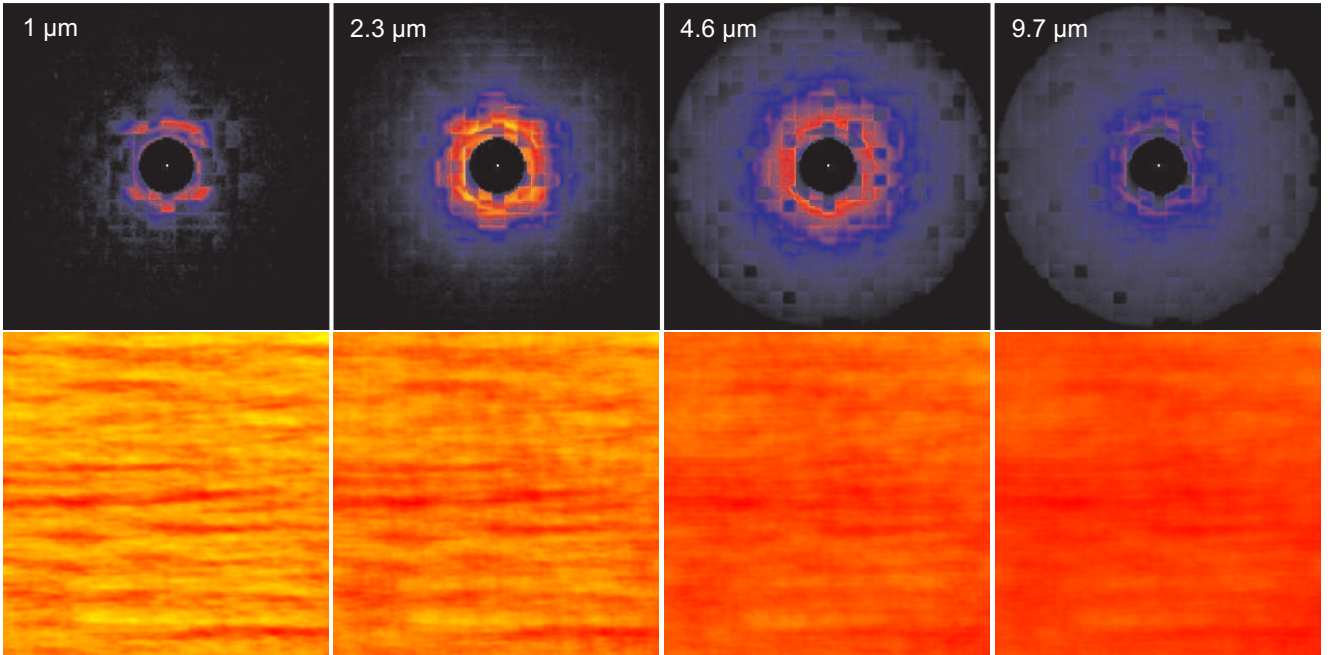


**Figure 2.** *Top row:* images of torus at different wavelengths, face-on view. From left to right, panels represent model images at 1, 2.3, 4.6, and 9.7  $\mu\text{m}$ . All images are given in the same, logarithmic color scale. The visible squared structure is due to the clumps which in our model are in the form of cubes. The adopted values of torus model parameters are: optical depth  $\tau_{9.7} = 5$ , dust distribution parameters  $p = 1$  and  $q = 2$ , the half opening angle  $\Theta = 50^\circ$ , the relative clump size  $\xi = 12.5$ , the inner and outer radius  $R_{\text{in}} = 0.8$  and  $R_{\text{out}} = 3$  pc, respectively. *Bottom row:* microlensing magnification maps after convolution with the corresponding tori images from the top row. Maps correspond to the region shown in the right panel of Fig. 1. For clarity, a different scale of coloring for each map is adopted, so that the details of each image are visible.

wavelength dependency of the torus size, the magnification amplitude of the microlensing events is also wavelength dependent. The magnification is highest at near-infrared wavelengths, decreasing toward the mid-infrared range, and remains almost constant in the far-infrared part of the SED. Note that, as the torus size is larger than the typical size of microlens  $R_E$ , its radiation will always be magnified by a certain factor. Therefore, in the right panel of Fig. 4 we also illustrate the amplitudes relative to the minimum, i.e. to the beginning of a HME.

We note here that, at near-infrared wavelengths, the accretion disk radiation may still have a significant contribution to the SED. As the accretion disk is much smaller than the typical size of  $R_E$ , it can lead to microlensing events of much higher amplitudes and shorter timescales. However, in this work we investigate only the long-term variations caused by microlensing of the dusty torus; microlensing of the accretion disk has been thoroughly studied in the literature (e.g. Jovanović et al. 2008; Blackburne & Kochanek 2010; Morgan et al. 2010; Dexter & Agol 2011)

### 3.2.2 Dependence on torus parameters

The parameters that determine the viewing angle, the torus size, the dust distribution and the primary source luminosity, directly or indirectly, all contribute to the pattern of the torus IR emission and its apparent size at the given wavelength (Stalevski et al. 2012). Therefore, each of these parameters could affect the shape and amplitudes of microlensing light curves. We adopted a set of parameter values as the standard ( $p = 1, q = 2, \Theta = 50^\circ, R_{\text{out}} = 3 \text{ pc}, L = 10^{12} L_\odot$ ) and then we varied each of these parameters, while keeping the others constant. The resulting microlensing light curves for simulated magnification events at  $1 \mu\text{m}$  are shown in Fig. 5.

The outer radius of the torus has the largest impact on the magnification amplitude (see Fig. 4). Obviously, for smaller torus sizes, the magnification will be higher. The half opening angle ( $\Theta$ ) is another parameter which defines the size of torus, especially when seen edge-on. As expected, the tori with smaller opening angle will show larger variations under influence of microlensing.

It is evident that the viewing angle (inclination  $i$ ) also has a significant influence. The dust-free lines of sight (corresponding to the type 1 AGN;  $i = 0^\circ$ ) provide a direct view of the innermost region of very hot dust, which is obscured in the case of dust-intercepting lines of sight (type 2 AGN;  $i = 70, 90^\circ$ ). Thus, in the former case, the larger part of the emission we see is originating from a more compact region than in the latter case. As a result, the amplitudes of the magnification events will be higher in the case of type 1 objects.

The parameters  $p$  and  $q$  define the spatial distribution of the dust density (Eq. 2). The larger values correspond to the more compact distribution of the dust. However, from the panels in the bottom row of Fig. 5 we see that, although more compact dust configuration tend to have higher amplitudes, these parameters do not significantly influence microlensing light curves. This is because, for the adopted value of the primary source luminosity ( $L = 10^{12} L_\odot$ , typical for quasars), radiation is able to penetrate further into the dust, and thus diminish the difference between compact and extended dust distributions. In the case of  $\sim 10$  times smaller primary source luminosities, the dust distribution parameters do have a noticeable impact.

**Table 1.** Rise times for HMEs, in years, calculated for different values of lens redshift and transverse velocity of the lens. Source is fixed at redshift  $z_s = 2$ .

$z_l$	$v_l$ [km/s]		
	500	1000	2000
0.05	164	82	41
0.5	364	182	91

### 3.2.3 Timescales of microlensing events

To characterize timescales of high magnification events, we use the rise time – the time interval between the beginning and the peak of a microlensing event. We estimate the rise time by measuring the distance traveled by the source, relative to the caustics, from the beginning to the peak of HME, and divide it by the effective source velocity. The effective source velocity  $V$ , i. e. the velocity of the source relative to the caustics with time measured by the observer is given by the expression (Kayser et al. 1986)

$$\mathbf{V} = \frac{1}{1+z_l} \frac{D_{ls}}{D_l} \mathbf{v}_o - \frac{1}{1+z_l} \frac{D_s}{D_l} \mathbf{v}_l + \frac{1}{1+z_s} \mathbf{v}_s. \quad (11)$$

The source velocity  $\mathbf{v}_s$  and the lens velocity  $\mathbf{v}_l$  are measured in the source and lens plane, respectively, they are distance weighted, and, due to the redshifts, translated into the observer's frame. The transverse velocity of the observer  $\mathbf{v}_o$  can be determined from the dipole term in the microwave background radiation. With an amplitude of 387 km/s (e.g., Kogut et al. 1993), the observer's motion will be important for some lenses and unimportant for others, depending on the direction towards the source. For simplicity, we will assume here that the direction of the observer's motion is parallel to the direction towards the source, so the first term in the Eq. (11) can be neglected. Assuming that the peculiar velocities of the source and lens, in their own planes, are of the same order, the last term can be neglected as well. With these approximations, the effective source velocity is reduced to the expression

$$V \simeq \frac{1}{1+z_l} \frac{D_s}{D_l} v_l. \quad (12)$$

In the case of lensed system Q2237+0305, several studies found the transverse velocity of the lens to be in the range between approximately 500 and 2000 km/s (Wyithe et al. 1999; Kochanek 2004; Gil-Merino et al. 2005). We adopted three values in this range and calculated the corresponding effective source velocity and rise times of HMEs. In the Table 1, we present estimated rise times, in years, for the two prominent HMEs indicated in the Fig. 3 with a dotted line, for different values of lens redshift and transverse velocity of the lens. Depending on these parameters, the obtained rise times are in range from several decades to several hundreds of years.

### 3.2.4 Influence on entire IR SED

In Fig. 6 we illustrate the influence of microlensing on the entire dusty torus SED in the  $1\text{--}50 \mu\text{m}$  range. From this figure we see that there is a significant difference in the amount of overall flux between the SEDs when microlensing is absent (solid line) and those under the influence of microlensing (dashed and dotted lines). However, due to the large size, the torus will always cover a large area of a microlensing magnification pattern and it will always be magnified by a certain factor, so the difference between the SEDs



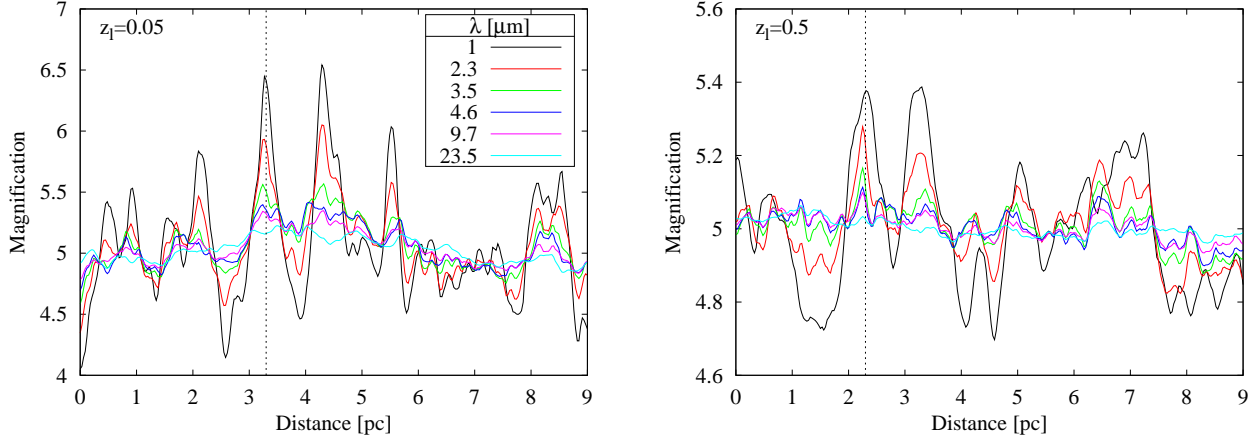


**Figure 3.** Light curves of magnification events at different rest-frame wavelengths (indicated in the legend), extracted from the magnification maps convolved with the corresponding images of tori. *Left panel:*  $z_l = 0.05$ . *Right panel:*  $z_l = 0.5$ . Note the different range of y axis shown in the two panels. The dotted line in both panels indicates two HMEs referenced throughout the text. The distance given in the x axis represents the distance crossed by the source, relative to the caustics, for the given values of the source and lens redshifts. The value “0” corresponds to the beginning of the path from which the lightcurve was extracted.

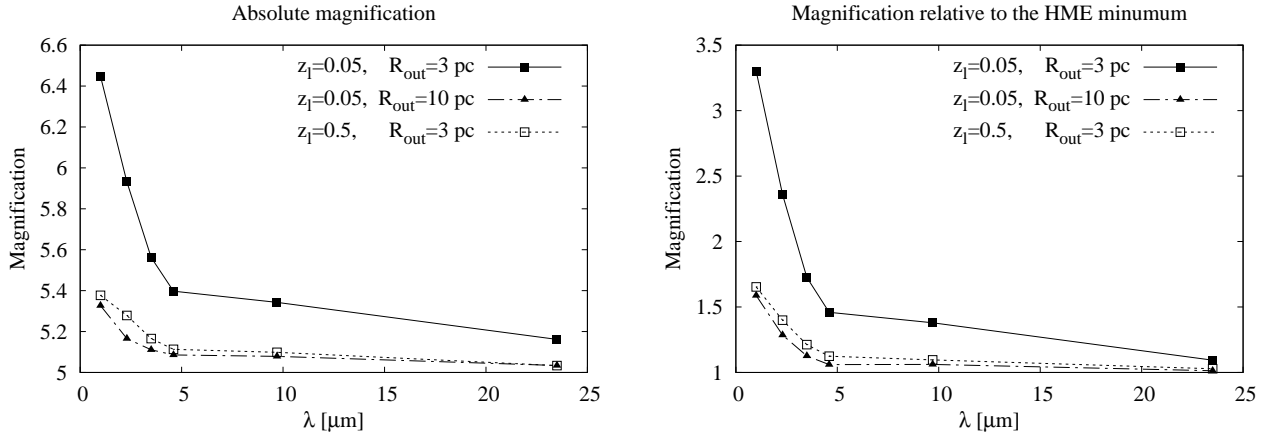


**Figure 4.** Magnification amplitude as a function of restframe wavelength, for prominent HMEs seen in Fig. 3. Full squares: HME peaking at  $\sim 3.3$  pc in left panel of Fig. 3 ( $z_l = 0.05$ ). Triangles: HME peaking at  $\sim 2.3$  pc in the right panel of Fig. 3 ( $z_l = 0.5$ ). Empty squares: the same as for the full squares, but for larger value of torus outer radius. *Left panel:* absolute magnification amplitude. *Right panel:* magnification amplitude relative to the minimum (beginning of the HME).

at the beginning (dashed line) and the peak (dotted line) of HME is marginal. Also, it is evident that HMEs do not change the shape of SED significantly.

#### 4 CONCLUSIONS

We investigated gravitational microlensing of AGN dusty tori in the case of lensed quasars. The dusty torus was modeled as a clumpy two-phase medium. The radiative transfer code SKIRT was used to obtain SEDs and images of the tori at different wavelengths. The ray-shooting technique has been used to calculate microlensing magnification maps. Due to the large dimensions of dusty tori (compared to the Einstein ring radius of the microlens in the source plane), they must be treated as extended sources. Thus, images of the tori were convolved with the magnification maps. We simulated microlensing by the stars in the lens galaxy, in the case of lensed quasars, for different configurations of the lensed system and dif-

ferent values of the torus parameters, in order to estimate (a) amplitudes and timescales of high magnification events, and (b) the influence of geometrical and physical properties of dusty tori on light curves in the infrared domain. From our investigation, we conclude the following.

- (i) Despite their large size, we found that AGN dusty torus could be significantly magnified by microlensing in some cases. The amplitude of magnification depends on wavelength, torus parameters, and configuration of the lensed system.
- (ii) The size of torus is wavelength dependent. As a consequence, the magnification amplitude of microlensing events is also wavelength dependent. The magnification is the highest in the near-infrared, decreases rapidly towards the mid-infrared range, and stays almost constant in the far-infrared part of SED.
- (iii) As microlensing is sensitive to the size of the source, pa-

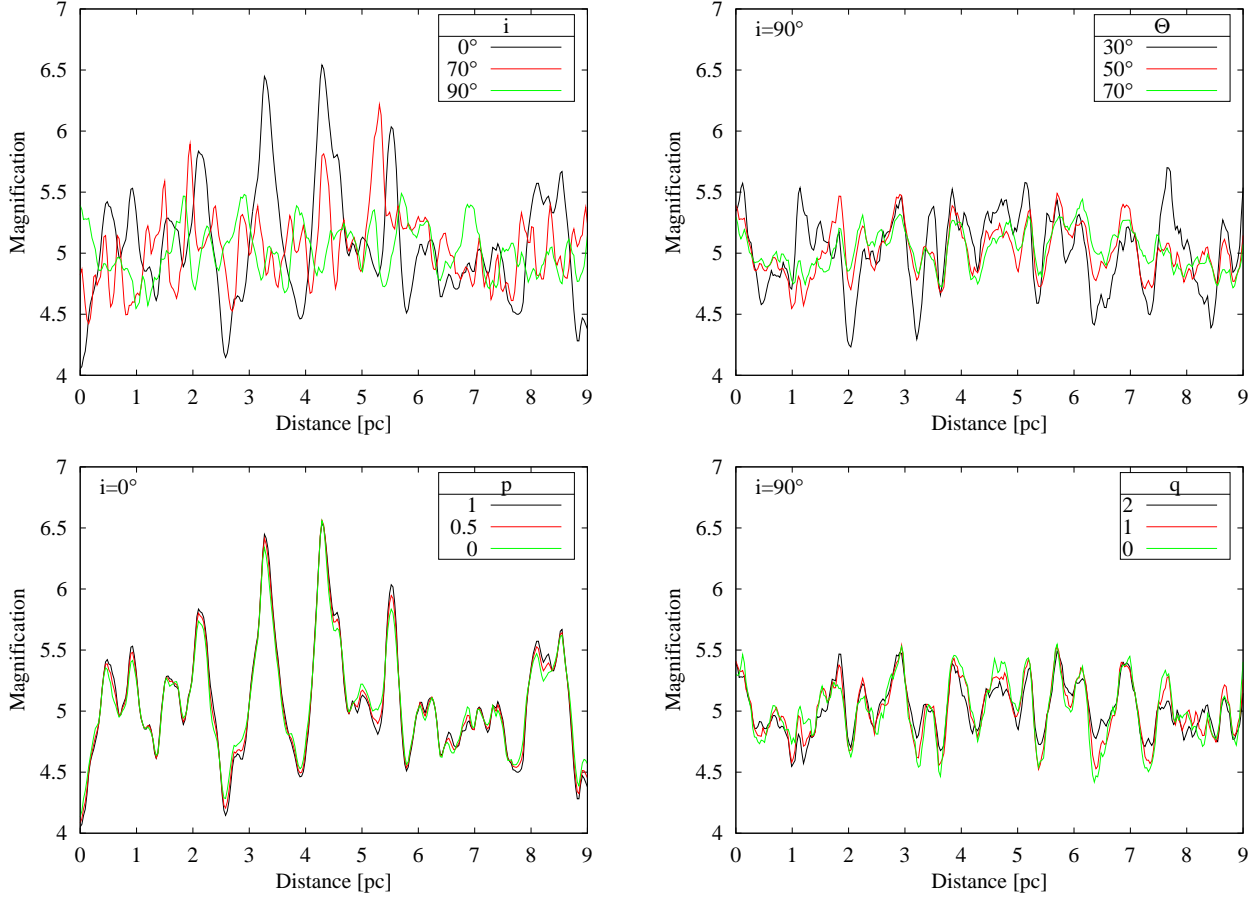


**Figure 5.** Microlensing light curves at  $1\ \mu\text{m}$  for the different parameters of the torus model. Upper left panel shows dependance on inclination, upper right panel on half opening angle, bottom panels on dust density distribution parameters. In all panels the black line corresponds to the most compact dust configuration, green line for the largest, and the red line for the intermediate.

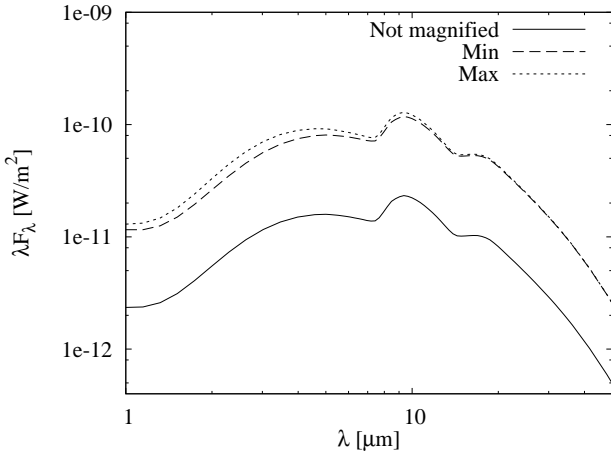


**Figure 6.** Dusty tori SEDs in  $1\text{--}50\ \mu\text{m}$  range. Solid line: not magnified. Dashed line: at the minimum of HME (at  $\sim 2.6\ \text{pc}$  in the left panel Fig. 3). Dotted line: at the maximum of HME (at  $\sim 3.3\ \text{pc}$  in the left panel Fig. 3). The parameters of the torus are the same as taken in Fig. 2.

rameters determining the geometry and the apparent size of the torus, have a very important role. Tori with  $R_{\text{out}} \lesssim 10\ \text{pc}$  could be appreciably microlensed.

More compact dust configurations (e.g. steeper radial density profiles) result in smaller tori and thus in higher magnification amplitudes. However, for primary source (accretion disk) luminosities typical for quasars ( $10^{12}\ L_{\odot}$ ), the influence of the dust distribution parameters is diminished, because the radiation is able to penetrate the dust further.

Tori seen at type 1 (dust-free) inclinations, which provide a direct view of the innermost, hottest region, are more magnified than those at type 2 (dust-intercepting) inclinations.

- (iv) Lensed quasar systems with the lens galaxy closer to the observer, will have higher magnification amplitudes, owing to their larger Einstein ring radius projection on the source plane.
- (v) Estimated rise times, between the beginning and the peak of HMEs, are in the range from several decades to several hundreds of years.

Given such long time-scales, microlensing would hardly prove to be a practical tool to study and constrain the properties of dusty tori, as it is in the case of AGN accretion disks. However, the results presented above should be kept in mind when investigating flux ratio anomaly of lensed quasar images in different wavelength bands. In such studies, it is important to determine the true magnification ratios between the images, in the absence of microlensing. In principle, this could be done by looking at the emission-line, infrared, and radio-emitting regions of quasars, as they all should be



large enough to safely disregard microlensing effects. However, we have shown that the infrared emission of dusty tori could be significantly microlensed in some cases, and thus, it is a less reliable tool for determining the “intrinsic” flux ratios.

## ACKNOWLEDGMENTS

This work was supported by the Ministry of Education and Science of the Republic of Serbia through the projects ‘Gravitation and the Large Scale Structure of the Universe’ (176003) and ‘Astrophysical Spectroscopy of Extragalactic Objects’ (176001).

## REFERENCES

- Abajas C., Mediavilla E., Muñoz J. A., Popović L. Č., Oscoz A., 2002, *ApJ*, 576, 640
- Agol E., Jones B., Blaes O., 2000, *ApJ*, 545, 657
- Agol E., Gogarten S. M., Gorjian V., Kimball A., 2009, *ApJ*, 697, 1010
- Alonso-Herrero A., Ramos Almeida C., Mason R., Asensio Ramos A., Roche P. F., Levenson N. A., Elitzur M., Packham C., Rodríguez Espinosa J. M., Young S., Díaz-Santos T., Pérez-García A. M., 2011, *ApJ*, 736, 82
- Baes M., Davies J. I., Dejonghe H., Sabatini S., Roberts S., Evans R., Linder S. M., Smith R. M., de Blok W. J. G., 2003, *MNRAS*, 343, 1081
- Baes M., Dejonghe, H., & Davies, J. I. 2005a, in Popescu C. C., Tuffs R. J., eds, *AIP Conf. Proc.*, The Spectral Energy Distributions of Gas-Rich Galaxies: Confronting Models with Data, 761, 27
- Baes M., Stamatellos, D., Davies, J. I., et al. 2005b, *NewA*, 10, 523
- Baes M., Fritz J., Gadotti D. A., Smith D. J. B., Dunne L., da Cunha E., Amblard A., et al. 2010, *A&A*, 518, L39
- Baes M., Verstappen J., De Looze I., Fritz J., Saffly W., Vidal Pérez E., Stalevski M., Valcke S., 2011, *ApJS*, 196, 22
- Barvainis R., 1987, *ApJ*, 320, 537
- Bate N. F., Floyd D. J. E., Webster R. L., Wyithe J. S. B., 2008, *MNRAS*, 391, 1955
- Blackburne, J. A., & Kochanek, C. S. 2010, *ApJ*, 718, 1079
- Blackburne J. A., Pooley D., Rappaport S., Schechter P. L., 2011, *ApJ*, 729, 34
- Chang, K., & Refsdal, S. 1979, *Nature*, 282, 561
- Chang, K., & Refsdal, S. 1984, *A&A*, 132, 168
- Chiba M., Minezaki T., Kashikawa N., Kataza H., Inoue K. T., 2005, *ApJ*, 627, 53
- Courbin, F., Saha, P., & Schechter, P. L. 2002, *Gravitational Lensing: An Astrophysical Tool*, 608, 1
- Dai X., Kochanek C. S., Chartas G., Kozłowski S., Morgan C. W., Garmire G., Agol E., 2010, *ApJ*, 709, 278
- Davis S. W., Laor A., 2011, *ApJ*, 728, 98
- de Looze I., Baes M., Zibetti S., Fritz J., Cortese L., Davies J. I., Verstappen J., et al. 2010, *A&A*, 518, L54
- Dexter, J., & Agol, E. 2011, *ApJL*, 727, L24
- Dobler G., Keeton C. R., 2006, *MNRAS*, 365, 1243
- Elíasdóttir, Á., Hjorth, J., Toft, S., Burud, I., & Paraficz, D. 2006, *ApJS*, 166, 443
- Fadely R., Keeton C. R., 2011, *AJ*, 141, 101
- Garsden, H., Bate, N. F., & Lewis, G. F. 2011, *MNRAS*, 418, 1012
- Gil-Merino R., Wambsganss J., Goicoechea L. J., Lewis G. F., 2005, *A&A*, 432, 83
- Goldberg D. M., Chessey M. K., Harris W. B., Richards G. T., 2010, *ApJ*, 715, 793
- Granato G. L., Danese L., 1994, *MNRAS*, 268, 235
- Inoue K. T., Chiba M., 2005, *ApJ*, 634, 77
- Jovanović P., Zakharov A. F., Popović L. Č., Petrović T., 2008, *MNRAS*, 386, 397
- Kayser R., Refsdal S., Stabell R., 1986, *A&A*, 166, 36
- Keeton C. R., Gaudi B. S., Petters A. O., 2003, *ApJ*, 598, 138
- Kochanek C. S., 1991, *ApJ*, 373, 354
- Kochanek C. S., 2004, *ApJ*, 605, 58
- Kogut A., Lineweaver C., Smoot G. F., Bennett C. L., Banday A., Boggess N. W., Cheng E. S., et al. 1993, *ApJ*, 419, 1
- Krolik J. H., Begelman M. C., 1988, *ApJ*, 329, 702
- Leipski C., Meisenheimer K., 2012, “The Central Kiloparsec in Galactic Nuclei (AHAR2011)”, *Journal of Physics: Conference Series (JPCS)*, IOP Publishing, ArXiv e-prints 1201.4773
- Mao, S., & Schneider, P. 1998, *MNRAS*, 295, 587
- Mathis J. S., Ruml W., Nordsieck K. H., 1977, *ApJ*, 217, 425
- Metcalf R. B., Madau P., 2001, *ApJ*, 563, 9
- Minezaki T., Chiba M., Kashikawa N., Inoue K. T., Kataza H., 2009, *ApJ*, 697, 610
- Morgan, C. W., Kochanek, C. S., Morgan, N. D., & Falco, E. E. 2010, *ApJ*, 712, 1129
- Mortonson M. J., Schechter P. L., Wambsganss J., 2005, *ApJ*, 628, 594
- Mosquera A. M., Muñoz J. A., Mediavilla E., 2009, *ApJ*, 691, 1292
- Mosquera A. M., Muñoz J. A., Mediavilla E., Kochanek C. S., 2011, *ApJ*, 728, 145
- Neugebauer G., Matthews K., 1999, *AJ*, 118, 35
- Popović L. Č., Mediavilla E. G., Jovanović P., Muñoz J. A., 2003, *A&A*, 398, 975
- Popović L. Č., Chartas G., 2005, *MNRAS*, 357, 135
- Popović L. Č., Jovanović P., Mediavilla E., Zakharov A. F., Abajas C., Muñoz J. A., Chartas G., 2006, *ApJ*, 637, 620
- Ramos Almeida C., Levenson N. A., Alonso-Herrero A., Asensio Ramos A., Rodríguez Espinosa J. M., Pérez García A. M., Packham C., Mason R., Radoski J. T., Díaz-Santos T., 2011, *ApJ*, 731, 92
- Schartmann M., Meisenheimer K., Camenzind M., Wolf S., Henning T., 2005, *A&A*, 437, 861
- Schneider, P., Ehlers, J., Falco, E.E. 1992, *Gravitational Lenses*, (Springer, Berlin)
- Schneider P., Weiss A., 1986, *A&A*, 164, 237
- Schneider P., Weiss A., 1987, *A&A*, 171, 49
- Schneider, P., & Wambsganss, J. 1990, *A&A*, 237, 42
- Sluse D., Claeskens J.-F., Altieri B., Cabanac R. A., Garcet O., Hutsemékers D., Jean C., Smette A., Surdej J., 2006, *A&A*, 449, 539
- Stalevski, M., Fritz, J., Baes, M., Nakos, T., & Popović, L. Č. 2012, *MNRAS*, 420, 2756
- Vidal E., Baes M., 2007, *Baltic Astronomy*, 16, 101
- Wambsganss J., Paczynski B., Katz N., 1990, *ApJ*, 352, 407
- Witt A. N., Gordon K. D., 1996, *ApJ*, 463, 681
- Wyithe J. S. B., Agol E., Fluke C. J., 2002, *MNRAS*, 331, 1041
- Wyithe J. S. B., Webster R. L., Turner E. L., 1999, *MNRAS*, 309, 261
- Xu D. D., Mao S., Cooper A. P., Wang J., Gao L., Frenk C. S., Springel V., 2010, *MNRAS*, 408, 1721
- Yonehara A., Hirashita H., Richter P., 2008, *A&A*, 478, 95

This paper has been typeset from a  $\text{T}_{\text{E}}\text{X}/\text{L}^{\text{A}}\text{T}_{\text{E}}\text{X}$  file prepared by the author.